Evaluation of lateral restraint in geosynthetic-stabilized base layers

S. Subramanian[1] and J. G. Zornberg[2]

[1]*The Transtec Group Inc., A Terracon Company, Austin, USA, E-mail: subu@thetranstecgroup.com*
[2]*Department of Civil, Architectural and Environmental Engineering, University of Texas at Austin, Austin, USA, E-mail: zornberg@mail.utexas.edu*

Received 01 May 2025, accepted 12 January 2026

ABSTRACT: Reduced-scale pavement test sections, with and without geogrid-stabilized base layers, were constructed and trafficked using a model Mobile Load Simulator (MLS11) to evaluate the mechanism of geogrid stabilization of unbound aggregate bases. The performance of the pavement sections was evaluated by measuring vertical surface displacements (rut), horizontal particle displacements within the base, and vertical stresses within the pavement structure. Two control sections, identical in their construction and configurations, were initially evaluated and found to produce repeatable performance, within 10% of each other, in terms of surface rutting, and horizontal particle displacements within the base. A geosynthetic-stabilized section, constructed with geogrid within the aggregate base, showed a 230% increase in traffic capacity compared to the control section at the same failure rut. The stabilized section also showed a 30% reduction in internal vertical stress at the middle of the base and a 17% reduction at the base-subgrade interface. The presence of the geogrid decreased the particle-to-particle shear transfer across the geogrid, which was observed as a reduction in particle displacements below the geogrid. The geogrid provided lateral restraint to offset the reduced shear transfer, the effects of which were observed from the redirection and reduction of lateral flow in the vicinity of the geogrid. The particle tracking sensors presented in this study proved to be a valuable tool to visualize the effect of lateral restraint provided by the geogrid, aiding understanding of this mechanism.

KEYWORDS: Geosynthetics, Accelerated pavement tests (APT), Geogrids, Lateral restraint, MLS11, Soil stabilization, Pavements & Roads

REFERENCE: Subramanian, S. and Zornberg, J. G. (2026). Evaluation of lateral restraint in geosynthetic-stabilized base layers. *Geosynthetics International.* [https://doi.org/10.1680/jgein.25.00066]

1. INTRODUCTION

Geosynthetics in roadway applications serve a variety of functions (Zornberg 2017; Giroud *et al.* 2023; Tutumluer *et al.* 2025), ranging from mechanical (such as separation, reinforcement, and stiffening functions) to hydraulic (such as lateral drainage, filtration, and moisture barrier capabilities). One common application of geosynthetics in flexible pavements is the mechanical stabilization of unbound aggregate layers (Byun *et al.* 2024; Robinson *et al.* 2025), which can be achieved through the stiffening function of geosynthetics (Zornberg 2017). This application involves the inclusion of geosynthetics within the unbound aggregate layers (or at the interface between the unbound aggregate and subgrade layers) and aims to improve aggregate layer performance by increasing its resilient modulus and, consequently, its structural capacity (Tutumluer *et al.* 2025; Wang *et al.* 2025 2024). The stiffening provided by the geosynthetic improves the properties of the unbound aggregates by creating a composite of the aggregates with the geosynthetic, whose performance is dependent on the stiffness of the soil-geosynthetic composite. This effect kicks in from smaller deformation levels of the soil–geosynthetic composite and thus helps mitigate the time-dependent decrease in modulus of the unbound aggregate layer. As a consequence, the stabilized aggregate layer experiences significantly less permanent deformation under repeated traffic loading than non-stabilized soil, contributing to an extended service life of the road (Zornberg 2017; Giroud *et al.* 2023).

Several mechanisms have been proposed in the literature since the 1970 s (Bender and Barenberg 1978; Haliburton *et al.* 1981; Perkins and Ismeik 1997; Al-Qadi *et al.* 2008; Zornberg and Gupta 2010) to explain how geosynthetics improve the performance of unbound aggregate layers in roadways. These mechanisms can be broadly classified into those triggered by large deformations (tensioned-membrane effect and increased bearing capacity) and those triggered by small deformations (lateral restraint). Since deformations in paved roads are limited by the serviceability criteria (rut depth), it is widely accepted that geosynthetic stabilization of unbound aggregates in flexible pavements must be achieved by "lateral restraint" (Sun and Han 2019; Giroud *et al.* 2023; Zornberg and Subramanian 2023; Tutumluer *et al.* 2025). Thus, "lateral restraint," which can be mobilized at relatively small displacements, has been recognized as the dominant mechanism for performance improvement in geosynthetic-stabilized paved roads (Perkins 1999; Christopher *et al.* 2008; Sun and Han 2019).

In a geosynthetic-stabilized aggregate layer, "Lateral restraint" may be defined as the mechanism by which the aggregate particles near a geosynthetic are restricted from lateral movements induced by traffic loads (Bender and Barenberg 1978; Holtz *et al.* 1998; Al-Qadi *et al.* 2008; Giroud *et al.* 2023; Tutumluer *et al.* 2025). This mitigation of movement, in the in-plane direction of the geosynthetic, is achieved through interlocking and/or friction between the aggregates and the geosynthetic (Zornberg and Gupta 2010; Kang *et al.* 2023). It involves transferring in-plane shear stresses within the soil matrix to the tension-bearing geosynthetic materials, which develop tensile forces. These tensile forces provide a confining effect, limiting the lateral movement of particles (via lateral restraint) in the vicinity of the geosynthetic and also limiting the transfer of shear stresses across the geogrid. Several studies have shown the effects of the lateral restraint developed as a modulus improvement in tri-axial samples (Wang *et al.* 2024) and large-scale beds (Wang *et al.* 2025), and as a reduction in vertical pressure or vertical deflections on top of the subgrade beneath the stabilized layer (Robinson *et al.* 2020). Further, mechanistic-empirical analysis methods for geogrid-stabilized systems based on lateral restraint have also been developed by Sun and Han (2019). However, studies experimentally demonstrating and visualizing the effects of lateral restraint (by direct measurement of particle movements) have not been reported in the technical literature. Direct measurement of lateral restraint can provide important insights into the understanding of the mechanism and its effects on particle displacement behavior within the pavement structure.

An important objective of this study is to experimentally demonstrate and quantify the lateral restraint mechanism by measuring and analyzing the horizontal displacement of particles in the aggregate bases of both geosynthetic-stabilized and control pavement sections subjected to rolling wheel loads. A unique experimental technique, involving an assembly of particle-tracking sensors, was developed as part of this study (Subramanian and Zornberg 2024), which is suitable for collecting the experimental data needed to generate the horizontal displacement field within the unbound aggregate base. Geosynthetic-stabilized and control pavement sections were constructed as part of this study and were trafficked to failure using a Mobile Load Simulator (MLS11). The horizontal displacements of particles within the aggregate base, vertical surface displacement at the pavement surface, and vertical stresses within the pavement structure were measured in both sections during trafficking. The repeatability of accelerated pavement tests is initially evaluated in this study by comparing the horizontal internal particle displacement and vertical surface displacement measurements of two non-stabilized (control) sections. Subsequently, the results from the stabilized section are compared to those from the non-stabilized sections to demonstrate the development of the lateral restraint mechanism. Overall, the methodology developed in this study was able to capture the mechanisms associated with geogrid-stabilized unbound aggregate base.

2. MATERIALS AND METHODS

2.1. Pavement layers

Three reduced-scale pavement sections (Control I, Control II, and Stabilized sections) were constructed as part of this study. The pavement model dimensions were adopted based on experimental considerations, such as accommodation of the loading equipment and mitigation of boundary effects. In particular, the study does not intend to reproduce a specific pavement prototype. As previously mentioned, the focus is instead on identifying governing mechanisms, namely, lateral restraint. Nonetheless, the scaling laws that apply to this physical model are discussed as follows. An approach to establishing the equivalence between the physical model and a prototype is to rely on the ratio between the standard load used as the basis for conventional design (40 kN) and the actual load applied in the physical model (2.1 kN). Accordingly, a ratio of 1:19 could be defined as a scaling factor for the applied load between the model and a full-scale prototype. The scaling factors used for the various other properties are shown in Table 1. To achieve 1:1 scaling of stresses and pavement layer moduli between the model and a full-scale section, the load and contact area were scaled by 1:19, while the thicknesses and stiffness were scaled by 1:4.36 ($=\sqrt{19}$). A commercially available geogrid with medium stiffness was used in this study and thus if scaled may represent a geogrid with stiffness that is on the high-end (or beyond) of those available in the market. The pavement layer

Table 1. Scaling factors used in this study

Property	Scaling factor (model: Prototype)
Stress	1:1
Modulus	1:1
Load	1:19
Contact Area	1:19
Thickness	1:4.36
Contact Radius	1:4.36
Stiffness	1:4.36

thicknesses used in this study conform to a scaled-down version of a typical pavement section adopted by TxDOT Austin District for new construction (TxDOT 2023). All three sections constructed in this study consisted of a 25-mm Hot Mix Asphalt (HMA) ride surface, 125-mm gravel base, and 150-mm sand subgrade resting on top of a bed of steel channels (shown in gray in Figure 1). The pavement layers were constructed above grade to facilitate access from the sides to the sensors within the pavement section and confined on all sides by a modular frame consisting of two 150-mm-tall steel channels stacked on top of each other (shown in orange in Figure 1). The pavement sections measured 1,800 mm in length and 1,200 mm in width, with a total height of 300 mm. The length of the pavement section was chosen to be 1800 mm to accommodate the longest section within the support structures of the MLS11. The width of the pavement section was selected based on pilot tests conducted with particle displacement measurements, where 1200 mm was found to be adequate for the particle displacements to sufficiently attenuate to zero before reaching the sides (about 150 mm from the sides). The height of the pavement section was selected based on typical recommendations of test pit depth to plate diameter (contact diameter of 65 mm) ratios for laboratory plate load tests of 4 to 6. This was later confirmed from the measurement of stresses at the bottom of the test sections where stresses below 3% of the applied stress were recorded. These stress measurements indicate that the effect of the boundary conditions on the performance of the test sections was negligible. A low-strength nonwoven geotextile was used to provide separation between the base and subgrade, preventing intermixing under compaction and trafficking. In the stabilized section, a biaxial geogrid was placed 75 mm below the HMA surface within the base to provide the stiffening function.

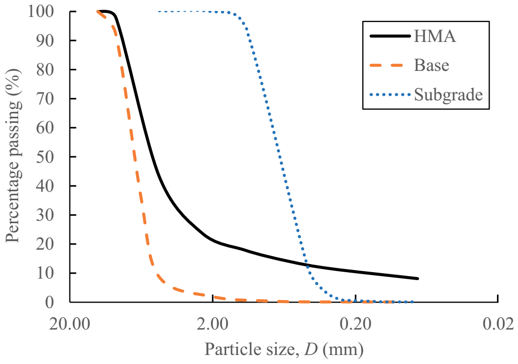

Figure 2. Grain size distribution of pavement materials

Table 2. Properties of base and subgrade used in this study

Commercial name	**Base**	**Subgrade**
	River-washed gravel (AASHTO #8)	Monterey sand (0/30)
Average Size, D_{50} (mm)	7.0	0.5
Coefficient of Uniformity, C_U	1.6	1.8
Coefficient of Curvature, C_C	1.0	1.0
ASTM Classification	GP	SP
Specific Gravity, G_s	2.650	2.655
Dry Unit Weight (γ_d), kN/m^3	17.1	15.4
Relative Density, RD (%)	85	67

As shown by the grain size distribution curves in Figure 2, both the base and subgrade consisted of uniformly graded soil with USCS classification of poorly graded gravel (GP) and sand (SP), respectively. The base aggregate is a river-washed pea gravel with a gradation conforming to AASHTO #8 aggregate size (AASHTO 2022), and the subgrade sand is a commercially available Monterey 0/30 sand. Table 2 summarizes the properties of the subgrade and base materials used in this study. Figure 3 shows the sequence of construction from the bottom of the subgrade to the asphalt ride-surface. The subgrade was placed in three 50-mm-thick lifts to a total thickness of 150 mm, whereas the base was placed in four 25-mm-thick lifts and two 12.5-mm-thick lifts to a total thickness of 125 mm. The weight of material (subgrade and base) required for each lift was calculated based on the volume of each lift and the target density. The calculated lift weight was divided into 12 equal parts, each placed in a 600 mm × 300 mm cell in

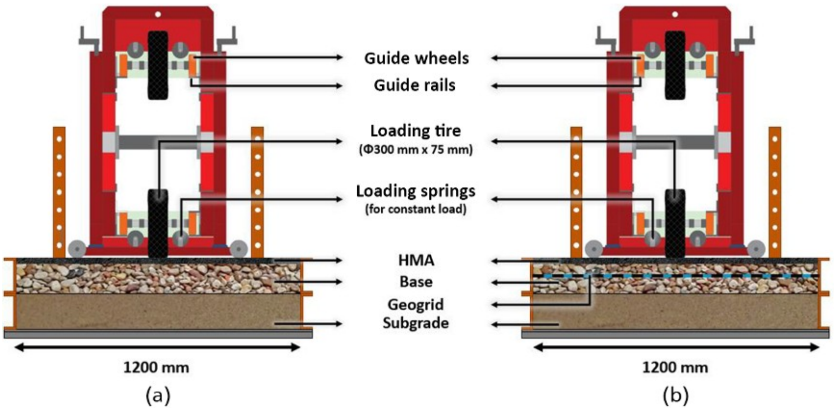

(a) (b)

Figure 1. Pavement test sections evaluated in this study: (a) Control I & II; and (b) Geosynthetic stabilized

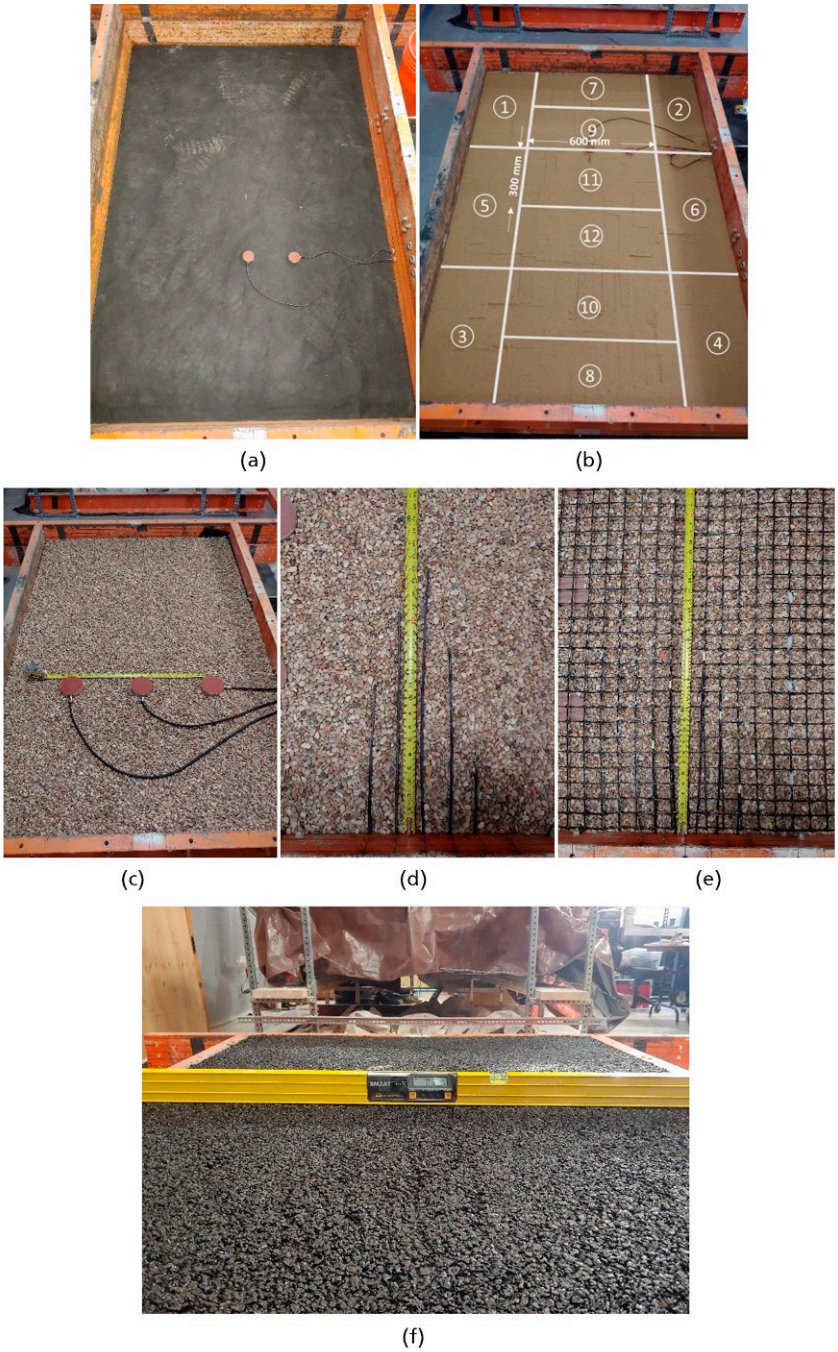

Figure 3. Construction sequence of a test section, showing the view of: (a) pressure cells at the bottom; (b) subgrade with pressure cells; (c) base with pressure cells; (d) particle tracking system within the base; (e) installed geogrid; (f) asphalt surface

the order shown in Figure 3(b). The placed material was compacted using hand tampers, and the compacted surface was checked with a straight edge and a level to ensure that the material had been compacted to the required height and was level. The compacted surface was scarified before the next lift was placed. A Dynatest LWD 3031 with a 150 mm base plate and 10 kg hammer was used with a modified drop height (300 mm) to measure the deflection under the impact load on top of the subgrade and each compacted lift of the base to ensure uniformity. The asphalt mixture used for the surface layer was a thin overlay mix (coarse – class A) conforming to TxDOT Special Specification 3239 (TxDOT 2004) with a binder content of 6.5%. The asphalt material was obtained pre-mixed from the asphalt plant, batched into 12 equal weights, and reheated in the oven to 165°C for 6 h. The hot asphalt was placed in the 12 cells in the same sequential order as the unbound materials and compacted using a plate vibrator, conducting 4 passes along the surface (Figure 3(f)). After the sections were trafficked, 9 samples were saw-cut from the asphalt layer. The uniformity of the asphalt layer was evaluated by measuring the density of the collected samples. The geogrid used for base stabilization in this study was an integrally formed, polypropylene, biaxial geogrid with aperture dimensions of 38 mm × 38 mm, installed at 75 mm from the top of the asphalt surface

(Figure 3(e)). The geogrid had similar tensile strength and stiffness properties in both the machine and cross-machine directions, as specified by the manufacturer. The manufacturer-specified Minimum Average Roll Value (MARV) for the unit tension at strains of 2% and 5% were 6.5 kN/m and 13 kN/m, respectively. The MARV for the ultimate tensile strength of the geogrid was specified as 20 kN/m.

2.2. Trafficking equipment

The pavement sections were trafficked with the MLS11 [previously referred to as MMLS3 in literature (Smit *et al.* 1999; Van de Ven and Smit 2000)]. The MLS11 is a reduced-scale accelerated wheel-loading device consisting of four loading tires connected to a chain of guide wheels. An electric motor drives the system of loading tires and guide wheels along rails in a vertical obround path, resulting in the application of repeated, unidirectional, rolling-wheel loads. The continuous circular motion of the loading tires allows for rapid application of loads up to 7,200 passes per hour, facilitating quick turnaround of tests. The rolling wheel loads are applied to the pavement surface by lowering the MLS11 onto the surface using four positioning screws at the ends. A spring and hinge mechanism attached to each loading tire ensures that the applied load remains constant within acceptable levels of surface displacement (up to 12 mm). The MLS11 is capable of applying a preconfigured load of 1.9 kN to 2.7 kN. For the three tests conducted in this study, the wheel load was set to 2.1 kN at a tire pressure of 620 kPa. As discussed earlier, the loading is scaled at 1:19 of a full-scale standard wheel load (40 kN). The MLS11 has been predominantly used to evaluate the performance of asphalt concrete mixtures used as surface layers in flexible pavements (Epps *et al.* 2001; Martin *et al.* 2003; Smit *et al.* 2003 1999). In the laboratory, the MLS11 has been used to determine the performance of bituminous mixtures in terms of their fatigue characteristics (Lee and Kim 2004; Bhattacharjee and Mallick 2012), rutting potential (Van de Ven *et al.* 1997; Lee *et al.* 2006a), and in the development of newer test methods for evaluation of surface treatment methods (Lee *et al.* 2006b). In the context of asphalt interlayers, several studies such as Baek (2020), Kim *et al.* (2009), and Raab *et al.* (2016) have conducted reduced-scale testing of asphalt concrete slabs with the MLS11 and were able to capture the mechanisms associated with the mitigation of fatigue cracks due to reinforcement of the asphalt surface layer with carbon-fiber reinforced plastics and geosynthetics. Lee *et al.* (2015) demonstrated the development of rut through the mechanism of shear flow in the HMA surface layer and its reduction due to the reinforcing geosynthetics by conducting reduced-scale tests on control and reinforced asphalt slabs using the MLS11. Limited research has been reported on the use of MLS11 and reduced-scale pavement testing to evaluate the mechanisms associated with stabilization of unbound aggregate layers. Tang *et al.* (2008) utilized the MLS11 to test reduced-scale pavement sections with geogrids to stabilize weak subgrade soil. The sections were instrumented with an LVDT to measure subgrade deflections, which were the researchers' primary performance metric. No studies on the geogrid-stabilization of unbound aggregate layers of reduced-scale flexible pavements have been reported in the literature. The comprehensively instrumented pavement sections reported in this paper address the perceived lack of validation of the mechanisms leading to the improved performance of geosynthetic-stabilized unbound aggregate layers.

2.3. Instrumentation

The performance of the pavement sections was evaluated by measuring surface ruts, internal particle displacements, and vertical stress distribution within the pavement structure, as follows:

1. The surface rut was determined by measuring the profile of the surface with a custom-built 2D laser profilometer. The manufacturer's calibration of the 2D-laser was verified using standard gauge blocks ranging from 1 mm to 25 mm, and the profilometer's measurements were validated by profiling along a straight edge, with and without gauge blocks attached to them. The surface profiles were measured along the three transverse locations (beginning, center, and end) shown in Figure 4. The ruts determined (at the beginning, center, and end) were averaged to determine the overall rut at a given number of passes. For the Control Section 1, pavement surface profiles were measured before the start of testing (0 passes), and after 100, 1000, 3000, 10000, and 20000 passes (end of testing). For the Control Section 2, pavement surface profiles were measured before the start of testing (0 passes), and after 100, 1000, 3000, 10 000, 20 000, and 30 000 passes (end of testing). For the Stabilized Section, the surface profiles were measured before the start of testing (0 passes), and after 100, 1000, 10 000, 30 000, and 82 500 (end of testing) passes. The number of passes at which to measure the profiles was determined such that they were as

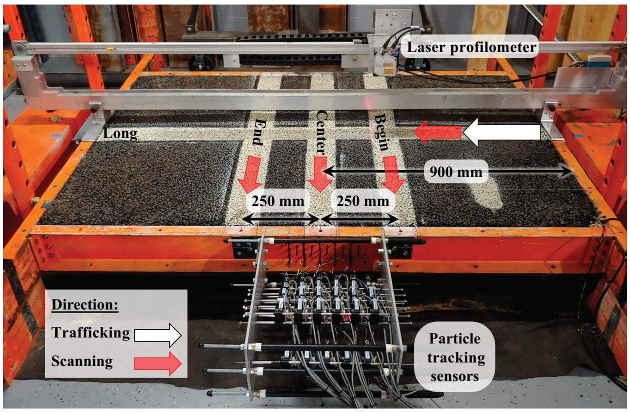

Figure 4. Instrumentation used to measure performance of the test sections: laser profilometer, particle tracking sensor array, and earth pressure cells (buried)

uniformly spaced as practically possible on the logarithmic scale. This was done to measure the primary (rapid deformation accumulation) and secondary (steady-state deformation accumulation) phases of the rut development process. These profiles were used to determine the rut at the selected intervals of trafficking for the two control sections and one stabilized section.

2. The lateral displacements of aggregate particles within the base due to the rolling wheel loads were measured using a novel particle tracking system. This system consisted of an array of linear displacement sensors affixed to the side of the pavement structure and connected horizontally via a tell-tale wire to particles within the gravel matrix of the base. The tell-tale wires transferred the movements of the attached particles within the base layer to the externally affixed displacement sensors, which continuously recorded the horizontal displacements under trafficking. Each linear displacement sensor was externally calibrated by fixing the sensor to a base plate and connecting the sensor cable to a micrometer head with a measuring range of 0 to 50 mm. The measured output voltage was plotted against the measured micrometer reading, and a linear calibration was calculated. Figure 3(d) shows the staggered arrangement of tell-tales wired to particles within the base. The black housing cables are used to protect the tell-tale wires from damage during construction and to facilitate free movement as the particles displace. Figure 4 shows the particle tracking sensor array mounted on the side of the pavement section. Figure 5 displays the layout of the trackable particles installed within the base of the control and stabilized sections. The internal particle displacements measured by this system were used to generate displacement fields, normal strain fields, vertical displacement gradient fields, and volumetric dilation. These results ultimately helped identify the development of restraint by the geogrid against internal particle movements.

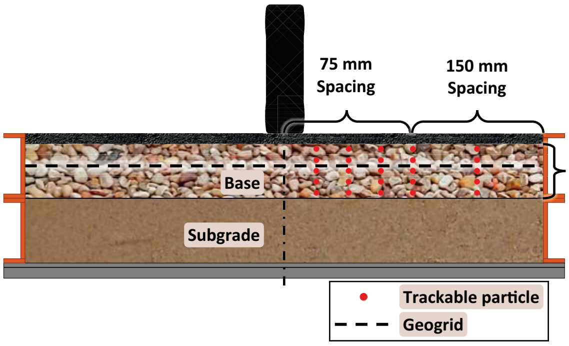

Figure 5. Cross-section showing the layout of trackable artificial particles

3. The vertical compressive stresses within the pavement structure were measured using earth pressure cells (EPCs) at mid-depth within the base (Figure 3(c)), at the top of the subgrade (Figure 3(b)), and at the bottom of the subgrade (Figure 3(a)). Figure 6 shows the schematic of the location of the EPCs within the two pavement cross-sections. These locations were chosen to determine stress redistribution within the soil-geogrid composite (base mid-depth), stress reduction on top of the subgrade, and the extent of the boundary effects (bottom of the subgrade). The horizontal spacing of the EPCs was adopted to maximize coverage within the width of the test section. The EPCs were calibrated using static loads: in isolation, under 1” padded cushioning, and embedded 1” deep within a sample box filled with the subgrade/base material. The tests with padded cushioning closely followed the manufacturer’s calibration results. In contrast, the tests with embedded sensors showed a stress level higher than the applied stress (by 20%) due to arching of the cohesionless soil under the rigid plate. For the purposes of this study, the manufacturer’s calibration values were used since it was challenging to recreate the material and loading conditions during trafficking in the sample box. The dynamic increase in vertical stress under trafficking was recorded continuously for the duration of the test. These results were used to develop plots of stress distribution within the pavement structure.

The instrumentation setup showing the array of particle tracking sensors and the laser profilometer performing a longitudinal profile is shown in Figure 4. Additional information on the development of the instrumentation system (for rut, particle displacement, and internal stresses), along with the data collection, processing, and analysis, can be found in Subramanian and Zornberg (2024).

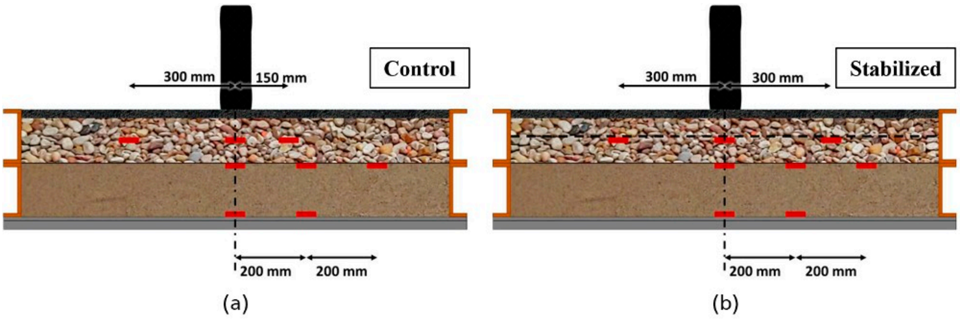

Figure 6. Cross-sections showing the locations of pressure cells in: (a) control section; and (b) stabilized section

3. RESULTS AND DISCUSSION

The measured responses of the two control sections and the stabilized section subjected to rolling-wheel loads (with no lateral wander) of the MLS11 are discussed in this section.

3.1. Geogrid-induced reduction in surface deformation

The ruts measured with increasing wheel passes in the two control (C-1 and C-2) sections and the stabilized (S) section are presented in Figure 7. The good agreement between the results obtained in the two control sections, indicated by dashed lines, square (C-1) and triangular (C-2) markers, demonstrates the repeatability of the accelerated pavement tests performed as part of this study. The two control sections were found to perform within 10% of each other in terms of surface rut after a given number of wheel passes, while the stabilized section performed significantly better than the control sections. The 10% discrepancy between the two control section repeats (C-1 and C-2) is deemed acceptable for the purposes of this study.

Although the surface profiles, and hence rut magnitudes, were obtained at discrete intervals of wheel passes during testing, the rut curve (as a function of number of wheel passes) can be used to estimate the rut on the pavement surface at any given number of wheel passes, N, through interpolation. Thus, given a failure rut depth, r, the number of passes to failure, N_r, for any pavement section can be readily obtained using the rut curves. For example, the number of passes to failure, N_r, at a failure rut depth ($r = 12.5$ mm) for the two control sections and the stabilized section can be determined as illustrated in Figure 7. The two control sections reached a rut of 12.5 mm after about 12,000 passes, while the stabilized section was subjected to over 40,000 passes before reaching the same rut. This corresponds to a 230% improvement in performance in the stabilized section compared to the 10% variability amongst the control sections. Since the geometry, materials, and construction of the control and stabilized sections were essentially identical in all aspects except the stabilizing geogrid, the improved performance of the stabilized section is a direct result of the stabilization provided by the geogrid.

To quantify the improvement in pavement performance resulting from the stabilizing geogrid, the concept of Traffic Benefit Ratio (TBR) is utilized herein. AASHTO (2009) defines the TBR as the ratio of the number of load cycles (wheel passes) in a stabilized pavement structure to reach a defined failure state to the number of load cycles for a control section to reach the same defined failure state. By definition, TBR is the function of the defined failure state, that is failure rut in this study, and thus, for different failure rut values, the TBR can be determined as a function of the pavement rut, r. Figure 8 shows the TBR of the stabilized section compared against the two control sections (S/C-1 and S/C-2 – solid lines) for various levels of failure rut, r_f. It also shows the control sections compared against each other (C-1/C-2 and C-2/C-1 – dashed lines) to further illustrate the repeatability in terms of the TBR curves. The traffic ratio determined amongst the control sections remained very close to the ideal value of 1.0 (perfect repeats), with the most significant deviation occurring at the lowest failure rut measurement of 2.5 mm, where the likelihood of rut measurement errors is highest. The TBR of the stabilized section compared with the two control sections (C-1 and C-2) rises sharply to a maximum value of 4 and 5 for a rut of 3 mm and then decreases with increasing rut depth to a constant asymptotic value of 3.2 and 3.5, respectively. Thus, the stabilized section performed on average 3.3 times better than the control sections. An increase in traffic capacity of the pavement section due to geosynthetic stabilization of the unbound aggregate base has been widely reported in the literature. Abu-Farsakh *et al.* (2019) conducted accelerated moving-wheel load tests on identical pavement sections with and without geogrid stabilization of the aggregate base in the field. They found that the stabilized section showed a traffic capacity 2.12 times that of the control section for a failure rut depth of 0.75 inches. In their full-scale laboratory evaluation of geogrid-stabilized bases in flexible pavements using accelerated plate load tests, Sharbaf and Ghafoori (2017)

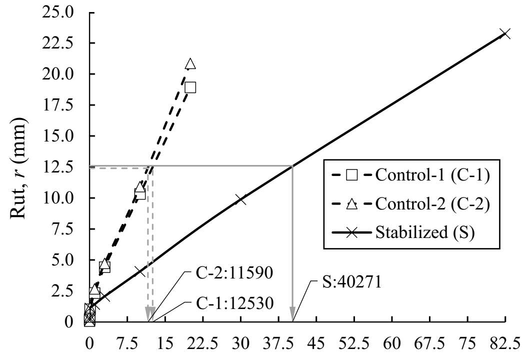

Figure 7. Rut, r, with increasing number of passes, N, in control (C-1 and C-2) and stabilized (S) sections

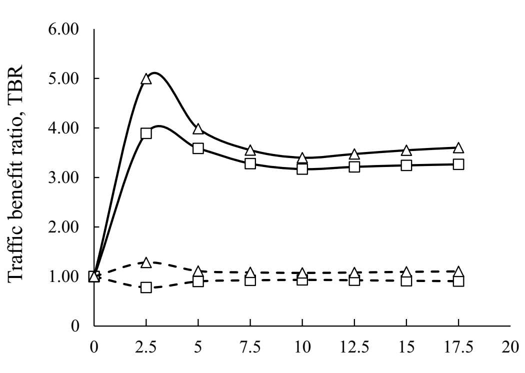

Figure 8. Traffic benefit ratio (TBR) as a function of failure rut, rf

found that the stabilization of the base with geogrid reduced the surface rutting or increased the traffic capacity by 4 times for smaller failure ruts and 2.2 times for larger failure ruts, which is similar to the observations presented in this study. Laboratory evaluation of 21 large-scale pavement sections with and without geogrid stabilization by Baadiga *et al.* (2023), over varying subgrade stiffnesses, showed that the representative value for TBR in stabilized-base design is between 1.5 and 4. Finite element analysis of flexible pavements with geogrid-stabilized base by Zadehmohamad *et al.* (2022) showed that the inclusion of the geogrid at the base-subgrade interface reduced the rate of pavement rutting and resulted in a TBR of 1.91 to 8.9, varying with the failure rut depth. Thus, the TBR obtained in this study is reasonably similar to that reported in the literature.

According to Transportation Research Board (2004), the development of rut in flexible pavements is attributed to two mechanisms: (1) one-dimensional densification or vertical compression; (2) two-dimensional plastic movement or lateral displacement under the wheel path. Since the material is not densified during lateral flow, it is associated with a characteristic heave on either side of the rut, which increases with rut depth while the width of the rut remains constant. Vertical compression is characterized by no heaving (since material is densified in-place) and an increase in rut width with trafficking. Figure 9 compares the surface profile shapes measured from the control and stabilized sections for the same vertical displacement under the wheel path ($w_{x=0\,mm}$). The x-axis shows the horizontal distance from the center of the wheel path (x), and the y-axis shows the vertical displacement of the surface (w) as measured by the profilometer. The surface profiles obtained from the control sections (C-1: blue and C-2:orange) at 1,000 (dotted), 3,000 (dashed) and 10,000 (solid) passes were compared with those obtained from the stabilized section (S: gray) at 3,000 (dotted), 10,000 (dashed) and 30,000 (solid) passes, so that the vertical displacement under the wheel path ($w_{x=0\,\mathrm{mm}}$) was the same for the control and stabilized section profiles being compared. For a given pavement section (control or stabilized), the surface profiles obtained at three different numbers of passes (dotted, dashed, and solid lines of the same color) were found to intersect approximately at a single point. This is represented by a solid circle of the same color in Figure 9, and corresponds to the location of near-zero vertical displacements (that is $w \cong 0\,\mathrm{mm}$ at these locations). These are the points around which the HMA surface pivots with an increasing number of wheel passes, resulting in heave on both sides of the wheel path. The location of these pivot points determines the width of the rut along the wheel path. As seen from Figure 9, the width of the rut remains constant in both the control and the stabilized sections. The existence of these points of zero vertical displacement and the near-constant rut width with increasing trafficking is consistent with the development of rut through the lateral flow of base materials as discussed earlier. This follows the fact that the base material was compacted to a high relative density of 85% and further densification under trafficking is unlikely due to the lack of significant confinement. This results in a short initial accumulation of shakedown rut (localized densification) followed by a near-linear progression of rut with increasing wheel passes. The pivot point (r) was located comparatively closer to the center of the wheel path in the stabilized section (at $x_r = 64\,\mathrm{mm}$) than in the control sections (at $x_r = 83.5\,\mathrm{mm}$ for both C-1 and C-2), implying a narrower width of the rut in the stabilized section compared to the control sections. The inclusion of geogrid along the radial flow of base aggregates redirected the flow, resulting in a narrowed rut path. Instead of a radially outward particle flow from the point of application of the wheel load, the particles tended to move outward (horizontally, parallel to the plane of the geogrid). With the geogrid laterally restraining the in-plane particle movement in its vicinity, the particles tend to move away from the geogrid (vertically) at locations away from the wheel path. Additionally, for the same vertical displacement under the wheel path ($w_{x=0\,\mathrm{mm}}$), the maximum heave (h) was comparatively higher and occurred closer to the wheel path in the stabilized section. In contrast, the maximum heave was comparatively smaller and occurred farther away from the wheel path in the control section.

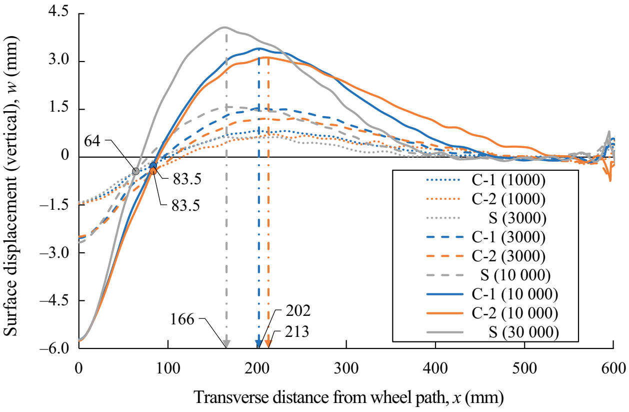

Figure 9. Surface profiles obtained for the control (C-1 and C-2) and stabilized (S) pavement sections

The estimated heave (h) as a percentage of the total rut (r) for various levels of rutting (in both the control and stabilized sections) is shown in Figure 10. As can be inferred from the results presented in Figures 9 and 10, the stabilized section exhibited a larger normalized heave compared to the control sections at all levels of rut (r). The magnitude of the normalized heave was found to increase with increasing rut depth, indicating that lateral flow became the dominant rut development mechanism at comparatively high rut levels. The magnitude of the heave is a function of the stress state adjacent to the wheel path. For the same vertical stress applied (by the wheel load), the higher the horizontal compressive stresses, the greater the tendency of the particles to heave (move vertically) instead of flowing laterally away from the point of application of the load. Thus, the higher heave in the stabilized section indicates a larger horizontal compressive stress adjacent to the

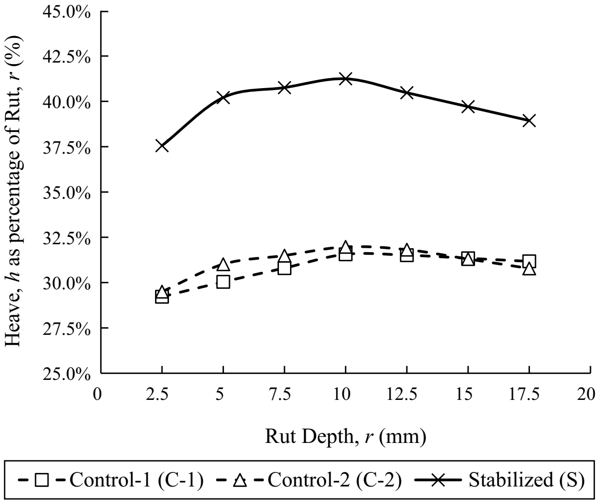

Figure 10. Normalized heave, h/r (%) for control and stabilized sections with increasing rut depth

wheel path compared to the control section. This increased horizontal compressive stress is caused by the development of tension in the stabilizing geogrid, which restrains the horizontal movement of particles and increases heaving.

3.2. Development of the lateral restraint mechanism

The lateral displacements measured by the particle tracking system were used to obtain the horizontal displacement field and the horizontal normal strain field within the base layer for the two control and stabilized sections. To assess the repeatability of the particle displacement measurements, the displacement fields obtained from the two control sections are compared in Figure 11. For illustrative purposes, the comparisons are made at three different stages of trafficking, namely after 3,000, 10,000 and 20,000 passes, to represent the pavement behavior at early, mid, and late stages in the life of the pavement sections. The x-axis of the contour plots shows the distance from the wheel path (x) in the transverse direction, with 0 mm at the center of the wheel path and 600 mm at the edge of the pavement model. The y-axis shows the depth from the surface (z) of the completed pavement section, with the HMA-base layer interface at 25 mm and base-subgrade interface at 150 mm. The contours represent horizontal displacements, with the darker regions corresponding to comparatively higher displacements. The displacement contours progressed from near the HMA-base interface to the bottom of the base layer with increasing surface rut due to trafficking. As expected, the contours show that the magnitude of lateral displacements increases with an increasing number of passes. The maximum lateral displacement within the base occurred towards the top of the base, about 150 mm from the center of the wheel path. The lateral displacements were found to decrease with depth within the base layer, and the location of the peak displacement (at a given depth) approaching the wheel path with increasing depth. As indicated by the results in Figure 10, the contours representing the displacement fields obtained from the two control sections are very similar, both in terms of their shape as well as the actual magnitude of the displacement contours. Section C-2 exhibited slightly higher displacements compared to C-1, which was consistent with the fact that Section C-2 also showed slightly higher levels of rut for the same number of passes (Figure 7) compared to Section C-1. Since the difference in the pavement surface rut and displacement contours at any given number of passes between the two control sections is notably smaller (an order of magnitude) than the corresponding difference between the stabilized and control sections, the lateral displacement measurements are deemed to have an acceptable level of repeatability for the purposes of this study.

Since the responses of both control sections are similar, only section C-1 is used for comparison with the stabilized section. To compare the displacement fields of the control and stabilized sections, two different approaches were adopted. The first approach involves comparing the displacement contours in the control and stabilized sections at a similar number of passes, that is a load-based approach. Figure 12 compares the displacement contours observed in the control and stabilized sections after 3,000, 10,000, and 20,000 passes. The depth of geogrid installation within the base is indicated by the dashed horizontal line (at $z = 75$ mm) in the displacement contours of the stabilized section. In the control section, the initial displacements under the wheel path were essentially vertical (i.e. near-zero horizontal displacement component under the wheel path) and flowed radially outward, peaking at a maximum horizontal displacement next to the wheel path. In the stabilized section, the inclusion of the geogrid within the path of this radial flow impedes particle movement, reducing the magnitude and redirecting the orientation of the lateral flow. The displacement contours appear vertically compressed and stretched out near the top of the base layer in the stabilized section compared to the control section. In the region close to the surface (above the elevation of the geogrid), the particle displacements were found to distribute over a comparatively larger area than in the control section due to the redirection of lateral flow, from a radial to a more horizontal direction away from the wheel path. Lateral displacements in the immediate vicinity of the geogrid (both above and below it) were significantly reduced. Such a reduction can be attributed to the aggregate particles being restrained by their interaction with the geogrid through interlocking and friction. Horizontal particle movements were also significantly reduced at all locations below the geogrid. Because of the presence of the geogrid, the lateral flow of particles due to traffic above the geogrid was not effectively transferred to the particles interlocked in the geogrid, which reduced the transfer of shear to the particles below the geogrid. Thus, the inclusion of a geogrid within an unbound aggregate layer in a flexible pavement results in: (1) redirection of the lateral flow above the geogrid over a wider distance from the wheel path; (2) lateral restraint of the unbound aggregates in the immediate vicinity of

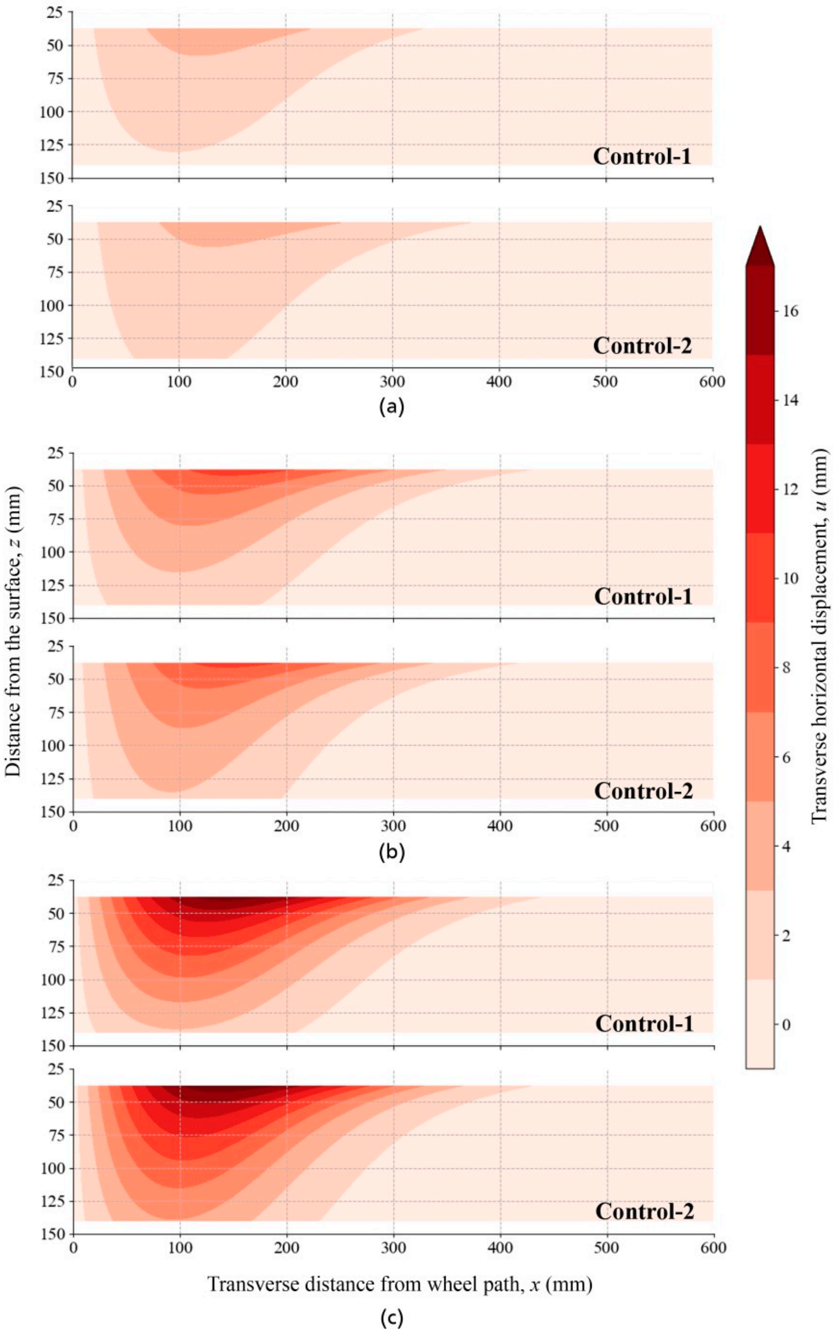

Figure 11. Lateral displacement fields in Control (C-1 and C-2) sections after: (a) 3000; (b) 10 000; and (c) 20 000 passes

the geogrid; and (3) reduced transfer of shear to the aggregate layer below the geogrid.

The second approach used to assess the displacements within the control and stabilized sections involved comparing the displacement contours at similar levels of vertical displacement along the wheel path ($w_{x=0\,\mathrm{mm}}$), that is a displacement-based approach. Figure 13 compares the lateral displacement contours of the particles in the base at vertical displacements (w) of 1.5 mm, 2.6 mm, and 5.7 mm under the wheel path ($x = 0$). The effects of lateral flow redirection and reduced shear transfer across the geogrid are observed in the contours of the stabilized section, which resulted in a wider distribution of lateral displacements above the geogrid. However, for the same level of vertical displacement under the wheel path, the lateral displacements observed above the geogrid location were higher in the stabilized than in the control section. In comparison, the displacements at locations below the geogrid were lower. Since the geogrid impeded the radial flow of the aggregates in the base, the particles above the geogrid were displaced farther to accommodate the same level of vertical displacement with reduced particle flow below the geogrid, resulting in increased lateral displacements above the geogrid. Also, increased lateral particle displacements were observed closer to the wheel path ($x = 0$ mm) in the stabilized section than in the control section, indicating that mostly vertical movement under the wheel path in the control section was redirected to lateral movement in the stabilized section parallel to the geogrid

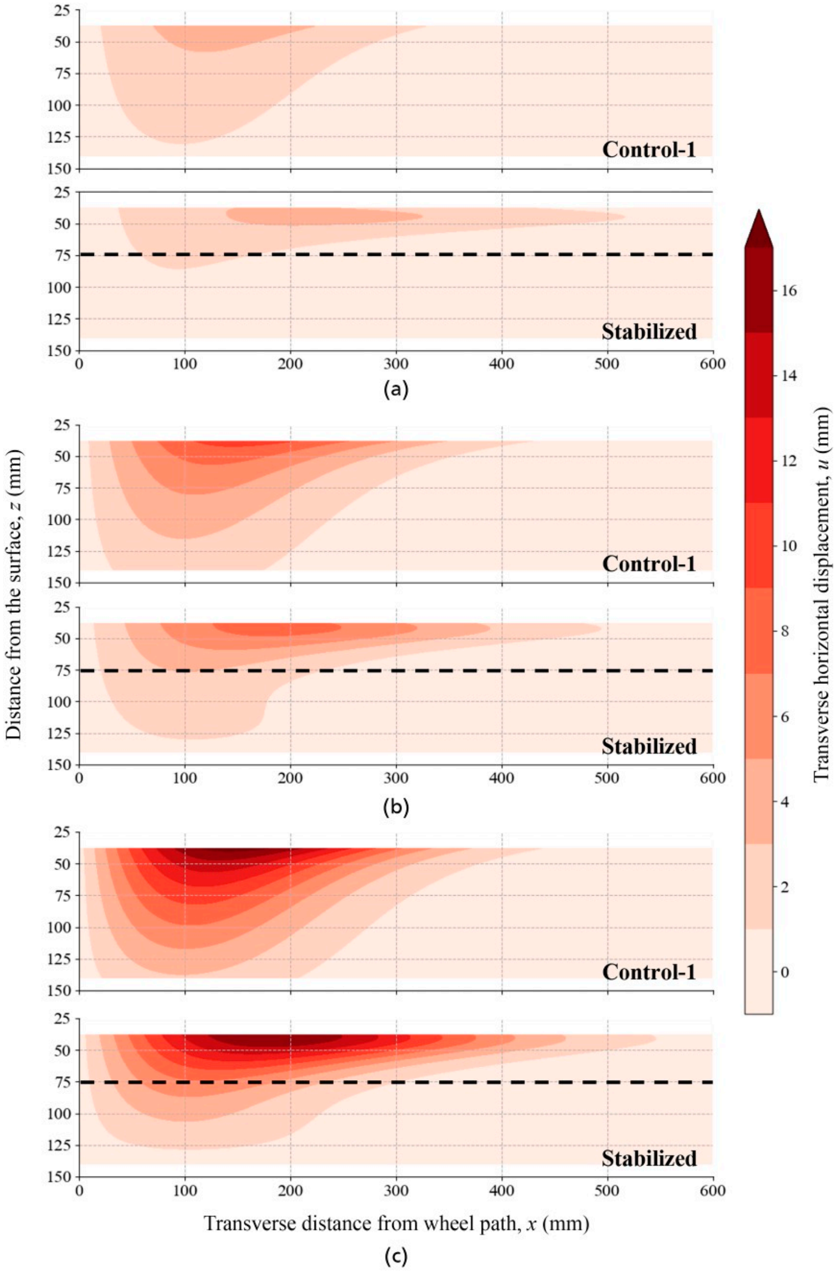

Figure 12. Lateral displacement fields in Control (C-1) and stabilized (S) sections after: (a) 3000; (b) 10 000; and (c) 20 000 passes

plane. This increased lateral displacement between the surface HMA layer and the geogrid resulted in a larger heave observed in the stabilized section for the same vertical displacement under the wheel path (Figure 9) compared to the control section. Thus, the presence of a geogrid was found to improve the rutting performance of the unbound aggregate layer by redirecting the radial flow path toward a more horizontal orientation and reducing the redirected lateral flow of aggregates by providing restraint against lateral movement through aggregate interlocking and friction.

Figure 14 shows the fields corresponding to the vertical gradient of lateral displacements in the control and stabilized sections. The vertical gradient, which is a component of the shear strain in the material, helps quantify the effectiveness of shear transfer from one aggregate to another immediately below it since it measures the change in lateral displacement with increasing depth. A smaller gradient (lighter contour) implies low relative displacement between adjacent aggregates along the depth, indicating an effective transfer of shear. In contrast, a steeper gradient (darker contour) represents a larger relative displacement between adjacent aggregates with depth. At comparatively low traffic levels (e.g. $n = 3{,}000$ passes), when cumulative plastic deformations are low, the light contour lines show a comparatively high shear transfer efficiency. With an increasing number of cycles, the shear transfer efficiency was found to decrease in the regions of large lateral flow. Thus, in the stabilized section, the shear transfer efficiency was lower than in the control section in the regions above the geogrid, characterized by more significant lateral flow (due to redirection), while the efficiency was higher than in the control section below the geogrid location.

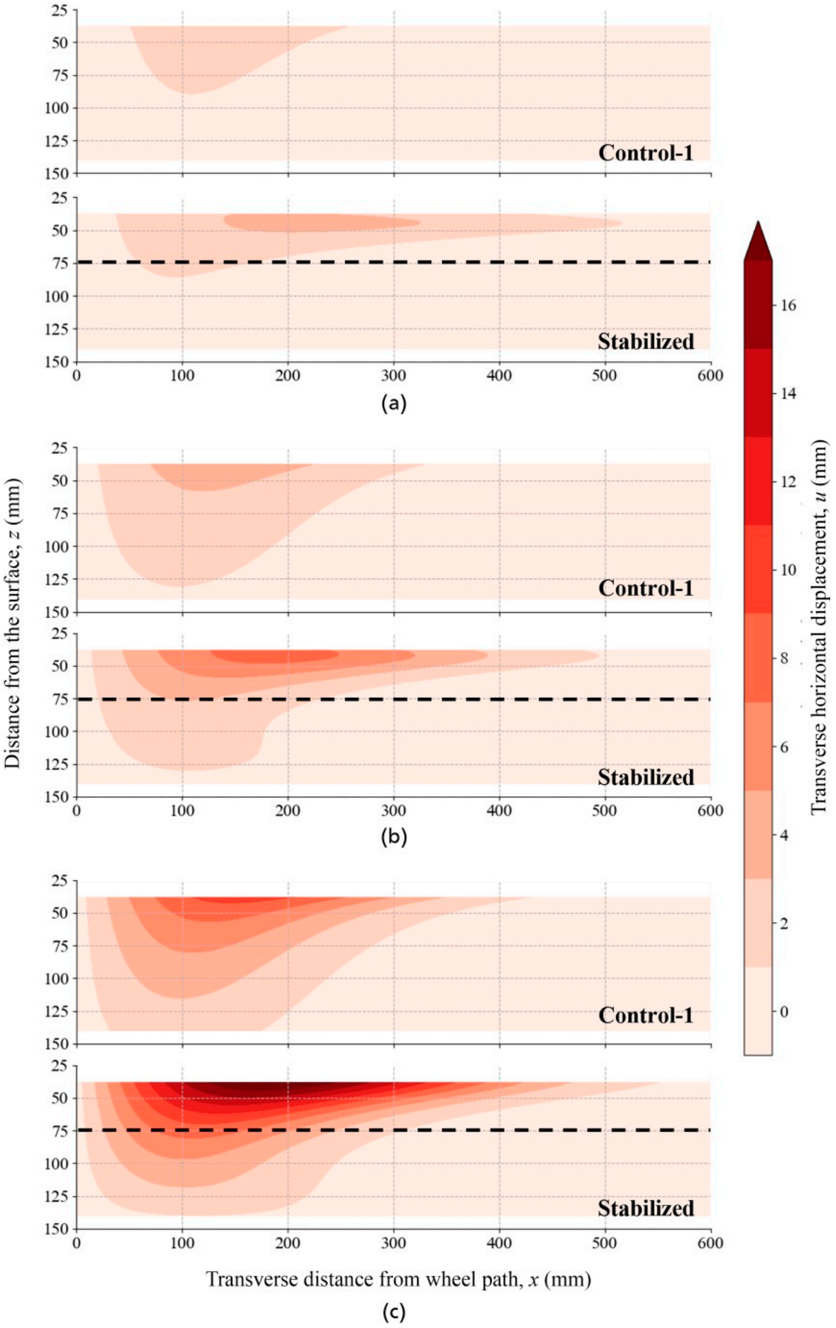

Figure 13. Lateral displacement fields in control (C-1) and stabilized (S) sections at vertical displacement under wheel path (wx = 0 mm) of: (a) 1.5 mm; (b) 2.6 mm; and (c) 5.7 mm

The traffic-induced horizontal normal strains within the base layer were determined as the partial derivative of the traffic-induced horizontal displacement field with respect to the transverse distance from the wheel path, x. Figure 15 compares the horizontal normal strain (ε_x) contours in the base of the control and stabilized sections obtained from the partial derivative of the displacement contours after 3,000, 10,000 and 20,000 passes. The region where strains are tensile is shown in red contours, and compressive strains are represented by blue contours. Regions with comparatively large strains are shown using a darker shade of red or blue, with the white contour representing a region of negligible strain. In both the control and stabilized sections, the region under the wheel path ($x = 0$ mm) showed the maximum tensile strain, which decreased with depth. Adjacent to the tensile region under the wheel path is a region of negligible strain (white contour), which marks the location of maximum horizontal displacement and the transition from a tensile region under the wheel path to a compressive region away from the wheel path. Although the magnitudes of tensile and compressive strains increased with increasing number of passes, the regions of tension and compression, and that of negligible strain, remained reasonably constant with increasing traffic in both the stabilized and control sections. The normal strains induced within the geogrid-stabilized base were lower than those induced in the control

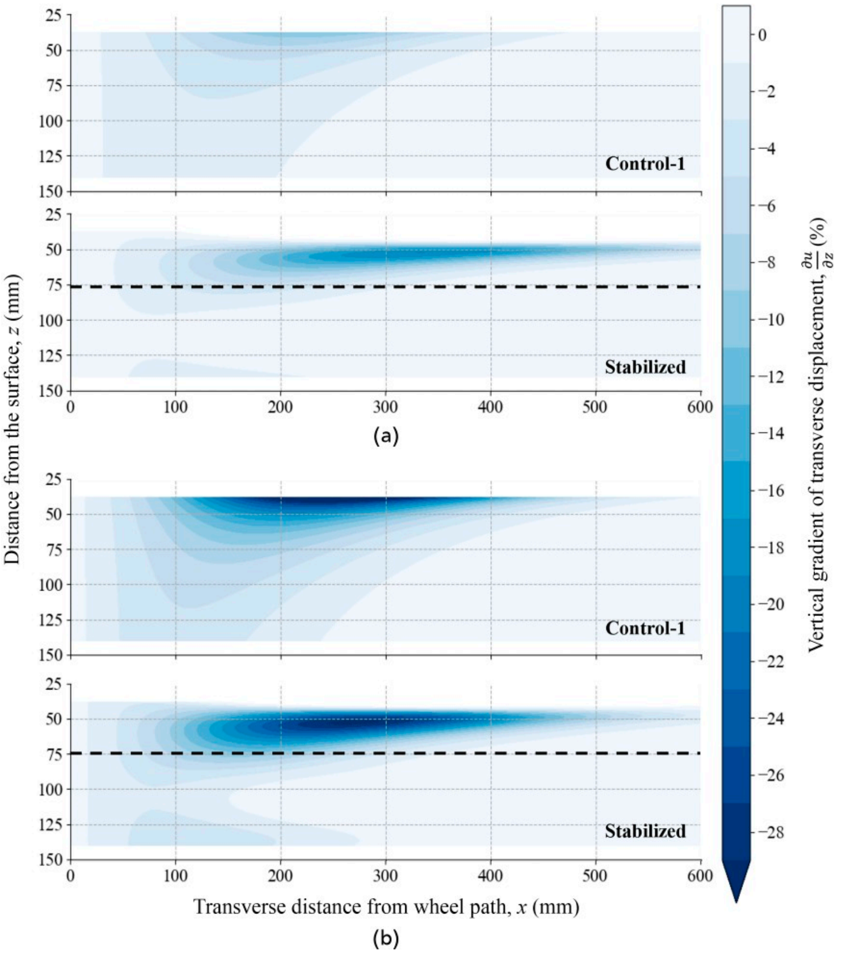

Figure 14. Gradient of lateral displacement field in control (C-1) and stabilized (S) sections after: (a) 3000; and (b) 10 000 passes

section for the same number of passes due to the lateral restraint effect. The stabilization of the base by the geogrid also reduced the depth to which the normal strains were induced due to the external wheel load. Finally, due to the redirection of lateral flow by the geogrid and the reduced shear transfer across the geogrid in the stabilized section, the strains induced (both compressive and tensile) were distributed over a wider area in the region above the geogrid and over a narrower area in the region below the geogrid. Figure 16 compares the horizontal normal strain contours for the control and stabilized sections at the same vertical displacement (w) at the surface along the center of the wheel path ($x = 0\,\text{mm}$). Since the geogrid stabilization reduced the depth of influence of the external load, the vertical displacements are accommodated by increased tensile strains under the wheel path in the stabilized section. This, in turn, resulted in an increase in compressive strains adjacent to the wheel path, which led to increased heave in the stabilized section for the same vertical displacement along the wheel path.

Post-trafficking forensic trenching of the control and stabilized pavement sections at the end of testing showed no changes in the thickness of the subgrade and HMA layers. Thus, the surface displacement measured by the profilometer can be assumed to equal the change in thickness of the base layer across the pavement section. This change in base layer thickness can be normalized with the initial base layer thickness (125 mm) to obtain the average vertical normal strain over the thickness of the base for an increasing number of passes. The horizontal normal strain fields, such as those shown in Figure 15, were used to determine the average horizontal normal strain over the thickness of the base at any distance from the center of the wheel path. If plane strain conditions are assumed, the volumetric strain, averaged over the depth of the base as a function of the transverse distance from the wheel path, equals the sum of the vertical and horizontal normal strains. Since tensile strains are assumed to be positive, a positive volumetric strain indicates dilation. Figure 17 presents the results of a volumetric strain analysis on the control section after 100, 1000, 3000, 10 000, and 20 000 passes as dashed lines. Since the surface rut in the stabilized section was not measured after 20 000 passes, the volumetric strains after 100, 1000, 3000, 10 000, and 30 000 passes are shown as solid lines instead for the stabilized section. Overall, the base aggregates exhibited a dilatant behavior, which is expected due to the high relative density (85%) at which the base was placed during construction of the pavement section. For a similar number of passes, the control section showed a greater tendency for dilation than the stabilized section. For similar levels of vertical displacement under the wheel path ($w_{x=0\,\text{mm}}$), that is

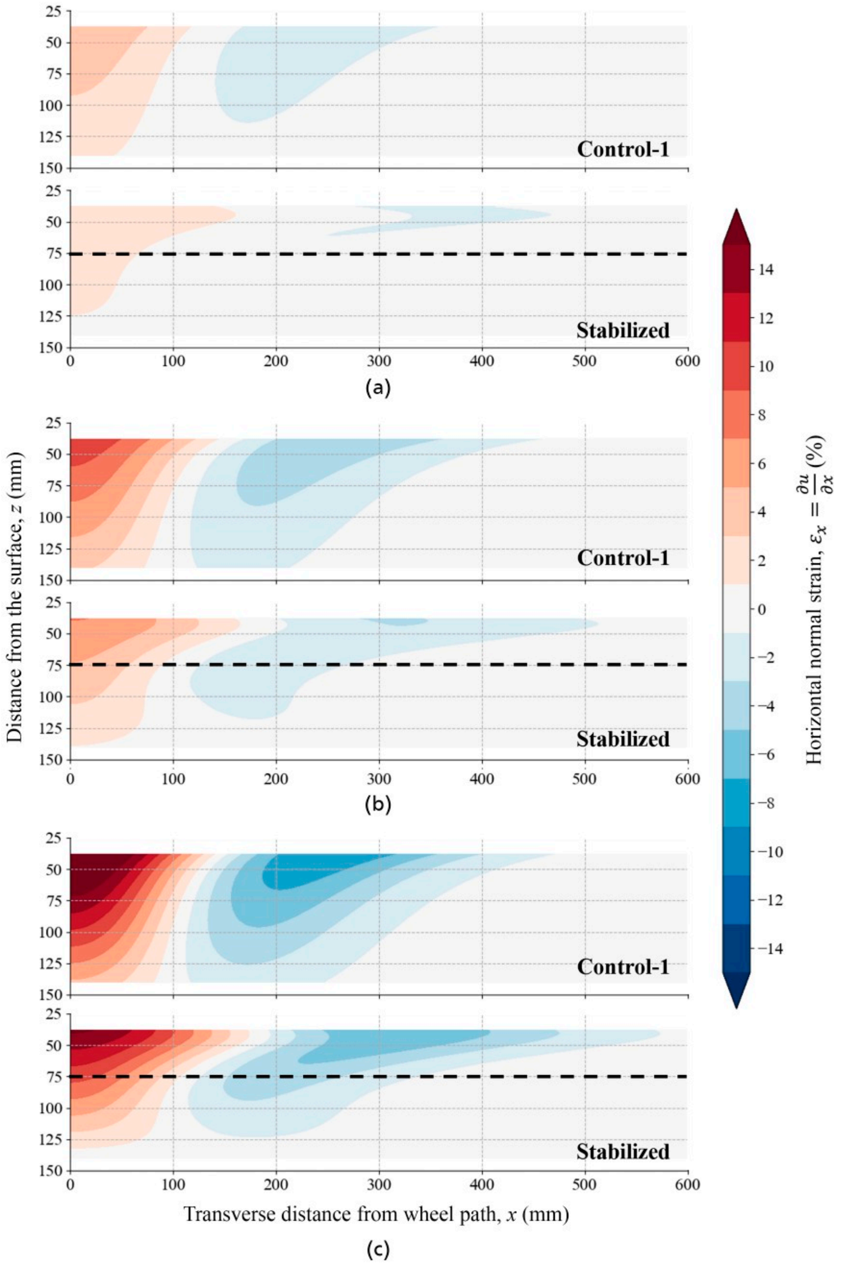

Figure 15. Fields of changes in horizontal normal strains in control (C-1) and stabilized (S) sections after: (a) 3000; (b) 10 000; and (c) 20 000 passes

comparing curves 1000 (C) – 3000 (S), 3000 (C) – 10 000 (S), and 10 000 (C) – 30 000 (S), the stabilized section showed more significant dilation than the control section. The dilation in the control section was comparatively more uniform with distance from the wheel path, whereas the dilation in the stabilized section quickly reduced to zero with increasing distance. This implies that volume changes in the control section were more evenly distributed across the width of the pavement section, whereas they were comparatively localized in the stabilized section, resulting in a narrower rut path and larger heave (Figure 9). After 30 000 passes, the stabilized section exhibited some contractive behavior far away from the wheel path, between 300 mm and 400 mm, corresponding to the location of maximum compressive strains in the normal strain field (Figure 16(c)).

3.3. Distribution of vertical stresses

From the continuously monitored response of the earth pressure cells, the increase in vertical stresses due to wheel loading was determined. This traffic-induced vertical stress within the pavement structure did not significantly change with increasing number of passes, in both the control and stabilized sections. The typical dynamic increase in stress recorded around the 3000th wheel pass in the control and stabilized sections is compared in Figure 18. The y-axis shows the traffic-induced vertical stress recorded by the earth pressure cells at various depths within the pavement structure, and the x-axis shows the transverse distance from the center of the wheel path at which the earth pressure cells were installed. The square, triangular, and circular markers represent the earth pressure cells installed at mid-depth

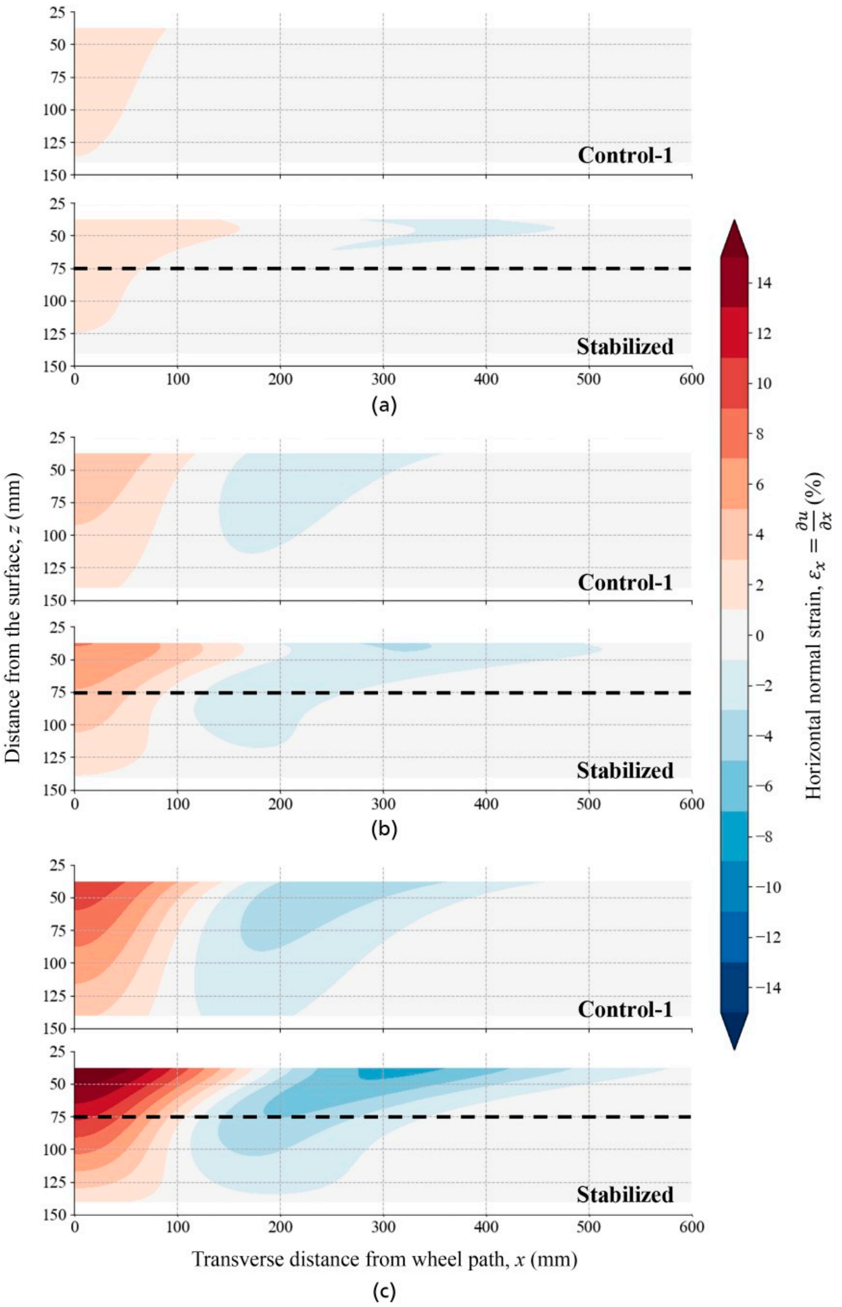

Figure 16. Fields of changes in horizontal normal strains in control (C-1) and stabilized (S) sections at: (a) 1.5 mm; (b) 2.6 mm; and (c) 5.7 mm vertical displacement along wheel path (wx = 0 mm)

in the base, at the base-subgrade interface, and at the bottom of the subgrade, respectively. The hollow markers represent the traffic-induced stress increase measured in the control section, and the solid markers represent those in the stabilized section. The vertical stress under the center of the wheel path in both the control and stabilized sections decreased with increasing depth, due to the distribution of the applied load over a wider area. Furthermore, the stress responses measured in the stabilized section at the center of the wheel path were lower than those measured in the control section by 30% at mid-depth of the base, by 17% on top of the subgrade, and by 13% at the bottom of the test section. This indicated a wider distribution of the applied load in the stabilized section, attributed to an increased unbound aggregate layer modulus, induced in

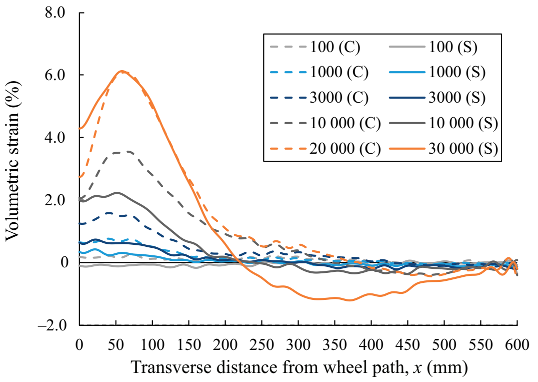

Figure 17. Volumetric strain with increasing number of passes in control (C-1) [dashed] and stabilized (S) [solid] sections

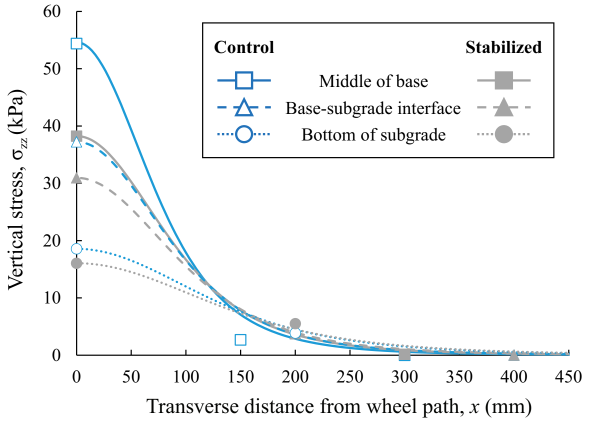

Figure 18. Vertical stress distribution after approximately 3000 passes in control and stabilized sections

turn by an increased confinement. This effect is less significant with increasing depth from the geogrid location, since the composite layer's increased moduli diminish with depth. Redistribution of the internal stresses due to the increased stiffness of the soil-geosynthetic composite layer has been widely reported in the literature. From the accelerated plate load tests conducted on full-scale laboratory pavement sections, Sharbaf and Ghafoori (2017) reported a 21% decrease in vertical stress on top of the subgrade (below the geogrid). Sun *et al.* (2017) conducted multi-stage cyclic plate load tests on top of unpaved, two-layer pavement systems with and without geogrid-stabilized bases of varying thicknesses. They found that the vertical stresses on top of the subgrade (immediately below the geogrid) decreased by 15% to 35% depending on the base thickness. In their layered-elastic analysis of pavement sections with stabilized aggregate base sub-layers, Byun *et al.* (2024) found that the improved moduli of the sub-layers due to the stabilization provided by the geogrid reduced the vertical stress on top of the subgrade by 8%. An important difference between the results reported in literature and in this study is the position of the geogrid. While all the previous studies discussed here were performed with the geogrid at the base-subgrade interface, the geogrid was installed within the base in this study, resulting in significant differences in stress distribution within the base layer. For instance, Byun *et al.* (2024) reported an increase in vertical stress at mid-depth of the base, since the sub-layering scheme allowed for a base layer with lower moduli overlying the geogrid-stabilized base with higher moduli. This effect was not observed in the current study, since all vertical stress measurements were made below the geogrid installation depth.

Table 3 compares the increase in traffic capacity (TBR) and the reduction in vertical stress on top of the subgrade observed in this study to those reported in literature. The observed results are comparable, indicating a similar macro response of geogrid-stabilized systems amongst these studies. However, the authors recognize that every study is different in terms of its pavement configuration, loading configuration, materials used, instrumentation deployed, and data reported. The results of this study are not meant to emulate a full-scale prototype using the physical model. For instance, a commercially available geogrid has been used in the model, resulting in a scenario where the geogrid is comparatively stiffer than they would be in potential prototypes. Thus, the results should not be used directly for design (e.g. by adopting the Traffic Benefit Ratios obtained in this study to predict the performance of a prototype). Instead, the study focuses on isolating the mechanism of lateral restraint (that has remained difficult to observe in previous field monitoring and experimental programs), quantifying and visualizing its effects on aggregate behavior within the pavement.

Table 3. Comparison of results with previously reported research

Study	Traffic benefit ratio	Stress reduction in subgrade
This Research	3.3	17%
Abu-Farsakh *et al.* (2019)	2.12	—
Sharbaf and Ghafoori (2017)	2.2 to 4	21%
Baadiga *et al.* (2023)	1.5 to 4	—
Zadehmohamad *et al.* (2022)	1.91 to 8.9	—
Sun *et al.* (2017)	—	15% to 35%
Byun *et al.* (2024)	—	8%

The discrete stress measurements within the control and stabilized sections at each depth were fitted with a parameterized form of the Boussinesq solution (Nwoji *et al.* 2017) for vertical stress distribution due to a point load (Subramanian and Zornberg 2024). The solid, dotted, and dashed lines in Figure 17 represent the best-fit curves for the vertical stress distribution at the middle of the base, base-subgrade interface, and bottom of the subgrade, respectively, with blue lines representing the control section and gray lines representing the stabilized section. The vertical stress decreased with depth under the wheel path, and it was distributed over a wider area at greater depths, resulting in increased vertical stress with depth at locations far from the wheel path ($x > 150$ mm). A wider distribution of vertical stress was also observed in the stabilized section, with lower vertical stress under the wheel path and increased vertical stress away from the wheel path, analogous to a pavement section with increased thickness. In fact, the stress distributions at mid-base in the stabilized section and on top of the subgrade in the control section were very similar. This indicated that the stabilized base with only thickness above the geogrid was able to achieve a stress distribution equivalent to that of the non-stabilized base with full thickness. This wider distribution of vertical stress within the base of the stabilized section is also observed to be compatible with the wider horizontal normal strain distribution (tensile region) under the wheel path when compared to the control section (Figure 15).

While the magnitude of horizontal strains increased with traffic, the zones of compression and tension in the horizontal normal strain contours remained constant and consistent with the vertical stress distribution, which also remained fairly unchanged throughout testing.

3.4. Behavior of geogrid-stabilized unbound aggregate base

The surface deformation of the two control sections, in this study, showed that the density, confining pressure, and stress state within aggregate base material were overall dilative in nature. This is inferred by the lack of 1-D densification under the wheel path in the rut curves (Figure 7), the development of heaves proportional to the rut (Figure 10), and the average volumetric dilation evaluations (Figure 17). Radial flow, such as that observed in the general bearing capacity failure of a shallow footing, is characterized by low horizontal displacements under the load (since movement is most vertical), high horizontal displacement at depths closer to the load (radial direction is outward near the surface), and lower horizontal displacements at depths far from the surface on which the load is applied (Terzaghi 1943). The lateral particle displacement fields observed in the control sections (Figure 11) conform to a section undergoing similar radial movement of particles away from the wheel path as the surface deforms under the applied load.

The inclusion of the geogrid within the aggregate base, in the stabilized section, disrupts this radial flow since the particles are no longer free to move across the geogrid. The particle movement must then be redirected laterally, as observed in the lateral displacement field contour plots, which show a wider displacement field than the control sections (Figure 12). However, the movement of the redirected particles is resisted by the interlocking of the particles within the aperture of the geogrid, friction against the geogrid, and the bearing of particles against those particles interlocked within the geogrid. Thus, the geogrid not only affects the stiffness of the soil in its immediate vicinity, but also of the soil in the region surrounding it (dubbed the geogrid influence zone, Byun *et al.* 2024), forming a soil-geosynthetic composite. The increased stiffness of this composite material is the key to the stabilization provided by geogrids for unbound aggregate bases. This resistance offered by the geogrid to the lateral particle movement by interlocking and/or shear is called lateral restraint.

This process induces tensile forces in the transverse ribs of the geogrid, which in turn provide a locked-in increase in horizontal confinement pressure. The effects of this lateral restraint are seen as (1) reduced particle displacements due to the resistance to horizontal movement in the lateral displacement fields (Figure 12); (2) increased heave due to redirection of the particle displacements from the horizontal to a vertically upward direction away from the geogrid due to the restriction of movement near the geogrid (Figure 10); (3) reduced dilation of the aggregate material due to the higher confinement pressure (Figure 17); (4) narrower rut path due to the higher confinement pressure (Figure 9); (5) redistribution of the vertical stresses over a wider area, resulting in reduced stresses below the geogrid installation depth (Figure 18). Since the tension in the geogrid would balance a part of the load-induced shear stresses from the particles above the geogrid, this would reduce the transfer of shear to the particles below the geogrid. This is directly observed as a reduction in the vertical gradient of transverse displacements in the immediate vicinity of the geogrid (Figure 14), resulting in reduced particle displacements below the geogrid (Figure 12).

Thus, lateral restraint results in (1) the redirection of particle movement within the aggregate base; (2) the restriction of lateral movement by interlocking/shear transfer; (3) the increase in confinement by development of locked-in tension; and (4) the reduction of shear transfer across the geogrid.

4. CONCLUSIONS

The APT program discussed in this study aimed at understanding the mechanisms involved in the geosynthetic stabilization of unbound aggregate layers in flexible pavements. The measurement of responses from two identical control sections helped establish the repeatability of the testing procedure. The development of lateral restraint was assessed by quantifying the reduction in lateral displacement of particles near the geogrid, as monitored by the particle-tracking sensors. The surface displacement profiles and vertical stress distribution within the pavement structure in the control and stabilized sections were also monitored and proved to be consistent with the internal particle displacements, aiding in understanding the pavement response to traffic. The key findings of the study are as follows:

- The experimental setup in this investigation was able to identify and quantify the restraint in lateral movements caused by the inclusion of geogrids. While the mechanism has been largely acknowledged for the improvement caused by geosynthetic base stabilization, it has not been previously experimentally observed.
- Geogrid stabilization of the unbound aggregate layer increased the flexible pavement's structural capacity, allowing for a 230% increase in traffic capacity for the conditions in this study. From the surface rut measurements, the stabilized section was found to produce shallower surface ruts compared to the control sections for a given number of passes.
- For similar vertical displacements under the wheel path, the presence of a geogrid within the base results in surface profiles of the stabilized section with a narrower rut valley and taller heaves compared to

those in the control sections. Specifically, the heave (h) as a fraction of the total rut (r) was found to be 20% higher in the stabilized section.

- The inclusion of a geogrid results in the redirection of the particle displacements from a radially outward direction to a horizontal direction within the base. It also results in the mitigation of the horizontal particle displacements near the geogrid due to the lateral restraint effect, and in the reduction of shear transfer across the geogrid.
- The improved modulus of the base, from the development of tension in the geogrid and the subsequent lateral restraint it provides, results in a wider distribution of the vertical stress and horizontal normal strains within the pavement structure. Lower peak stresses/strains under the wheel path and higher distributed stresses/strains away from the wheel path were observed in the stabilized section.
- The geogrid also provides strain relief as seen from the vertical gradient contours. This results in higher strains above (and lower strains below) the geogrid installation depth compared to those in the control section. These increased strain magnitudes closer to the surface result in taller heaves in the stabilized section.
- The increased confinement provided by the geogrid was found to lead to a reduction in the volumetric dilation of the base in the stabilized section.
- For base and subgrade material without fines and influence of moisture, the vertical stress distribution did not change with increasing number of passes.

DATA AVAILABILITY

All data, models, and code generated or used during the study appear in the submitted article.

FUNDING

The authors are indebted to the financial support provided by the Texas Department of Transportation (TxDOT). The technical insights provided by A. Smit and the support provided by M. Arellano and R. Phillips are gratefully acknowledged.

NOTATION

Basic SI units are shown in parentheses.

C_C	coefficient of curvature (dimensionless)
C_U	coefficient of uniformity (dimensionless)
D	particle diameter (m)
D_{50}	median particle diameter (m)
Gs	specific gravity (dimensionless)
h	heave above the initial asphalt surface due to rutting (m)
MARV	minimum average roll value (N/m)
N	number of wheel passes trafficked by the MLS11 (dimensionless)
N_r	number of wheel passes to failure (dimensionless)
RD	relative density (dimensionless)
r	rut measured at the surface of the asphalt layer (m)
r_f	rut depth used to define failure of the test section (m)
TBR	traffic benefit ratio (dimensionless)
u	horizontal displacement in the transverse direction (m)
w	vertical displacement of the surface (m)
$w_x = 0$	vertical displacement of the surface at the center of the wheel path (m)
x	transverse distance from the center of the wheel path (m)
z	vertical distance from the top of the asphalt surface (m)
γ_d	dry unit weight (N/m^3)
ε_x	normal strain in the transverse direction (dimensionless)
σ_{zz}	vertical normal stress within the pavement structure (Pa)

ABBREVIATIONS

AASHTO	American Association of State Highway and Transportation Officials
APT	accelerated pavement test
ASTM	American Society for Testing and Materials
C-1	Control Section – I
C-2	Control Section – II
EPC	earth pressure cell
HMA	hot mix asphalt
LVDT	linear variable displacement transducer
LWD	light weight deflectometer
MLS11	Mobile Load Simulator 11
MMLS3	model Mobile Load Simulator
S	stabilized section
TxDOT	Texas Department of Transportation
USCS	Unified Soil Classification System

REFERENCES

AASHTO (2009). AASHTO R50 Standard Practice for Geosynthetic Reinforcement of the Aggregate Base Course of Flexible Pavement Structures. AASHTO, Washington DC.

AASHTO (American Association of State Highway and Transportation Officials) (2022). AASHTO M43-05 Standard Specification for Sizes of Aggregate for Road and Bridge Construction. AASHTO, Washington DC.

Abu-Farsakh, M. Y., Chen, Q. & Hanandeh, S. (2019). *Accelerated Load Testing of Geosynthetic Base Reinforced/Stabilized Unpaved and Pavement Test Sections*, ROSAP.

Al-Qadi, I. L., Dessouky, S. H., Kwon, J. & Tutumluer, E. (2008). Geogrid in flexible pavements: Validated mechanism. *Transportation Research Record: Journal of the Transportation Research Board*, **2045**, No. 1, 102–109, 10.3141/2045-12.

Baadiga, R., Balunaini, U., Saride, S. & Madhav, M. R. (2023). Effect of geogrid type and subgrade strength on the traffic benefit ratio of flexible pavements. *Transportation Infrastructure Geotechnology*, **10**, No. 2, 180–210.

Baek, C. (2020). Performance evaluation of fiber-reinforced, stress relief asphalt layers to suppress reflective cracks. *Applied Sciences*, **10**, No. 21, 7701.

Bender, D. A. & Barenberg, E. J. (1978). *Design and behavior of soil-fabric-aggregate systems*, Transp. Res. Rec.

Bhattacharjee, S. & Mallick, R. B. (2012). Effect of temperature on fatigue performance of hot mix asphalt tested under model mobile load simulator. *International Journal of Pavement Engineering*, **13**, No. 2, 166–180, 10.1080/10298436.2011.653565.

Byun, Y.-H., Qamhia, I. I. A., Kang, M., Tutumluer, E. & Wayne, M. H. (2024). Modeling geogrid-stabilized aggregate base courses considering local stiffness enhancement. *Geosynthetics International*, **31**, No. 6, 888–897, 10.1680/jgein.23.00086.

Christopher, B. R., Cuelho, E. V. & Perkins, S. W. (2008). Development of geogrid junction strength requirements for reinforced roadway base design, In: *Proceedings of GeoAmericas 2008 Conference*, Cancun, Mexico. pp. 1003–1012.

Epps, A. L., Ahmed, T., Little, D. C. & Hugo, F. (2001). *Performance prediction with the MMLS3 at Westrack (Research Report No. FHWA/TX-01/2134-1*, Texas Transportation Institute, College Station, TX.

Giroud, J. P., Han, J., Tutumluer, E. & Dobie, M. J. D. (2023). The use of geosynthetics in roads. *Geosynthetics International*, **30**, No. 1, 47–80, 10.1680/jgein.21.00046.

Haliburton, T. A., Lawmaster, J. D. & McGuffey, V. C. (1981). *Use of Engineering Fabrics in Transportation-related Applications*, Haliburton Associates.

Holtz, R. D., Christopher, B. R. & Berg, R. R. (1998). Geosynthetic design and construction guidelines. *Participant Notebook. Nhi Course No*, **13213**, No. FHWA-HI-95–038.

Kang, M., Wang, H., Qamhia, I. I. A., Tutumluer, E. & Tingle, J. S. (2023). Local stiffness assessment of Geogrid-Stabilized unbound aggregates in a Large-Scale testbed. *Applied Sciences*, **14**, No. 1, 352, 10.3390/app14010352.

Kim, H., Sokolov, K., Poulikakos, L. D. & Partl, M. N. (2009). *Fatigue Evaluation of Carbon FRP-Reinforced Porous Asphalt Composite System Using a Model Mobile Load Simulator*, Transportation Research Record.

Lee, S. J. & Kim, Y. R. (2004). Development of fatigue cracking test protocol and life prediction methodology using the third scale model mobile loading simulator, In: *5th International RILEM Conference on Cracking in Pavements-Mitigation, Risk Assessment and Prevention*. pp. 29–36.

Lee, J., Kim, Y. R. & McGraw, E. O. (2006a). Performance evaluation of bituminous surface treatment using third-scale model mobile loading simulator. *Transportation Research Record: Journal of the Transportation Research Board*, **1958**, No. 1, 59–70.

Lee, S. J., Seo, Y. & Kim, Y. R. (2006b). Validation of material-level performance models: using the third-scale model mobile loading simulator. *Transportation Research Record: Journal of the Transportation Research Board*, **1949**, No. 1, 74–82.

Lee, J., Kim, Y. R. & Lee, J. (2015). Rutting performance evaluation of asphalt mix with different types of geosynthetics using MMLS3. *International Journal of Pavement Engineering*, **16**, No. 10, 894–905, 10.1080/10298436.2014.972916.

Martin, A. E., Walubita, L. F., Hugo, F. & Bangera, N. U. (2003). Pavement response and rutting for Full-Scale and scaled APT. *J. Transp. Eng. ASCE*, **129**, 11.

Nwoji, C. U., Onah, H. N., Mama, B. O. & Ike, C. C. (2017). Solution of elastic half space problem using boussinesq displacement potential functions. *Asian J. Appl. Sci*, **057**.

Perkins, S. W. & Ismeik, M. (1997). A synthesis and evaluation of Geosynthetic-Reinforced base layers in flexible Pavements- Part II. *Geosynthetics International*, **4**, No. 6, 605–621, 10.1680/gein.4.0107.

Perkins, S. W. (1999). *Geosynthetic Reinforcement of Flexible Pavements: Laboratory Based Pavement Test Sections (Research Report No. FHWA/MT-99-001/8138)*, Montana. Department of Transportation.

Raab, C., Arraigada, M. & Partl, M. N. (2016). Effect of reinforced asphalt pavements on reflective crack propagation and interlayer bonding performance. In *8th RILEM International Conference on Mechanisms of Cracking and Debonding in Pavements*, Springer, pp. 483–488.

Robinson, J. W., Tingle, J. S., Wayne, M. H., Kwon, J. & Norwood, G. (2020). Instrumentation response of Full-Scale multi-axial geogrid stabilized flexible pavements. In *Accelerated Pavement Testing to Transport Infrastructure Innovation*, Chabot, A., Hornych, P., Harvey, J. & Loria-Salazar, L. G., Editors, Springer International Publishing, Cham, pp. 564–573.

Robinson, W. J., Tingle, J. S., Tutumluer, E., Kang, M., Wayne, M. H. & Tamrakar, P. (2025). Using bender elements to investigate the effect of a multi-axial geogrid on aggregate layer stiffness. *Transportation Research Record: Journal of the Transportation Research Board*, **2679**, No. 1, 297–306, 10.1177/03611981231152465.

Sharbaf, M. & Ghafoori, N. (2017). Laboratory evaluation of triangular aperture geogrid reinforced flexible pavements. In *Bearing Capacity of Roads, Railways and Airfields*, CRC Press, pp. 1169–1176.

Smit, A., de, F., Hugo, F. & Epps, A. (1999). *Report on the first Jacksboro MMLS tests (Research Report No. FHWA/TX-00/0-1814-2)*, Center for Transportation Research, Austin, TX.

Smit, A., de, F., Hugo, F., Rand, D. & Powell, B. (2003). Model mobile load simulator testing at national center for asphalt technology test track. *Transp. Res. Rec*, **9**.

Subramanian, S. & Zornberg, J. G. (2024). Tracking particle displacements in unbound aggregate layers of roadways. *International Journal of Pavement Engineering*, **25**, No. 1, 2345786, 10.1080/10298436.2024.2345786.

Sun, X., Han, J. & Corey, R. (2017). Equivalent modulus of Geogrid-Stabilized granular base back-calculated using permanent deformation. *Journal of Geotechnical and Geoenvironmental Engineering*, **143**, No. 9, 06017012, 10.1061/(ASCE)GT.1943-5606.0001761.

Sun, X. & Han, J. (2019). Mechanistic-empirical analysis of geogrid-stabilized layered systems: Part I. Solutions. *Geosynthetics International*, **26**, No. 3, 273–285, 10.1680/jgein.19.00006.

Tang, X., Chehab, G. R. & Palomino, A. (2008). Evaluation of geogrids for stabilising weak pavement subgrade. *International Journal of Pavement Engineering*, **9**, No. 6, 413–429, 10.1080/10298430802279827.

Terzaghi, K. (1943). *Theoretical Soil Mechanics*, Wiley Online Library.

Transportation Research Board (2004). *Guide for Mechanistic–Empirical Design of New and Rehabilitated Pavement Structures. (Final Report No. NCHRP Project 1-37A)*, Transportation Research Board, National Research Council, Washington, D.C.

Tutumluer, E., Kang, M. & Qamhia, I. I. A. (2025). Geosynthetic stabilization of road pavements, railroads, and airfields. *Transportation Geotechnics*, **50**, 101321, 10.1016/j.trgeo.2024.101321.

TxDOT (2004). *SS3239 Special Specification for Thin Overlay Mix (TOM)*, TxDOT.

TxDOT (2023). *Austin District Pavement Design Standard Operating Procedures*, TxDOT.

Van de Ven, M., Smit, A., de, F., Lorio, R. & McGennis, R. (1997). Validation of some superpave design parameters by wheel testing with the scale model mobile load simulator, In: *Eighth International Conference on Asphalt Pavements*. Federal Highway Administration.

Van de Ven, M. & Smit, A. (2000). The Role of the MMLS Devices in APT, In: *South African Transport Conference. Presented at the Action in Transport for the New Millenium*, p. 16.

Wang, H., Kang, M., Kim, Y., Qamhia, I. I. A., Tutumluer, E. & Shoup, H. (2024). Geosynthetic-stabilized aggregate: quantitative modulus evaluation via bender element. *Geosynthetics International*, **32**, No. 5, 642–654, 10.1680/jgein.24.00078.

Wang, H., Kim, Y., Kang, M., Tutumluer, E. & Shoup, H. (2025). Geogrid stabilization effectiveness – comprehensive assessment through multiscale experiments with bender element sensor technology. *Geotextiles and Geomembranes*, **53**, No. 6, 1200–1214, 10.1016/j.geotexmem.2025.05.006.

Zadehmohamad, M., Luo, N., Abu-Farsakh, M. & Voyiadjis, G. (2022). Evaluating long-term benefits of geosynthetics in flexible pavements built over weak subgrades by finite element and mechanistic-empirical analyses. *Geotextiles and Geomembranes*, **50**, No. 3, 455–469.

Zornberg, J. G. & Gupta, R. (2010). Geosynthetics in pavements: North American contributions, in: Theme Speaker Lecture, Proceedings of the 9th International Conference on Geosynthetics, Guarujá, Brazil, pp. 379–400.

Zornberg, J. G. (2017). Functions and applications of geosynthetics in roadways. *Procedia Engineering*, **189**, 298–306, 10.1016/j.proeng.2017.05.048.

Zornberg, J. G. & Subramanian, S. (2023). Advances in the use of geosynthetics for stabilization of unbound aggregate layers, in. *E3S Web of Conferences*, **368**, 01003.

The Editor welcomes discussion on all papers published in Geosynthetics International. Please email your contribution to discussion@geosynthetics-international.com